

From imaginary to real chemical potential QCD with functional methods

Julian Bernhardt^{1,2,*} and Christian S. Fischer^{1,2,†}

¹*Institut für Theoretische Physik, Justus-Liebig-Universität Gießen, 35392 Gießen, Germany*

²*Helmholtz Forschungsakademie Hessen für FAIR (HFHF), GSI Helmholtzzentrum für Schwerionenforschung, Campus Gießen, 35392 Gießen, Germany*

We investigate the quality of the extrapolation procedure employed in Ref. [1] to extract the crossover line at real chemical potential from lattice data at imaginary potential. To this end we employ a functional approach that does not suffer from the sign problem. We utilize a well-studied combination of lattice Yang–Mills theory with a truncated set of Dyson–Schwinger equations in Landau gauge for $2 + 1$ quark flavors. This system predicts a critical endpoint at moderate temperatures and rather large (real) chemical potential with a curvature of the pseudo-critical transition line comparable to recent lattice extrapolations. We determine the light quark condensate and chiral susceptibility at imaginary chemical potentials and perform an analytic continuation along the lines described in [1]. We find that the analytically continued crossover line agrees very well (within one percent) with the explicitly calculated one for chemical potentials up to about 80 % of the one of the critical end point. The method breaks down in the region where the chiral susceptibility as a function of the condensate cannot any longer be well described by a polynomial.

I. INTRODUCTION

One of the major goals in studying the QCD phase diagram is to extract a quantitative understanding of the existence, the location and the properties of a critical endpoint (CEP). Observables connected to the appearance of the CEP have been probed in heavy-ion-collision experiments at RHIC/BNL [2] and HADES (FAIR Phase-0) [3], and will be explored in detail in the future CBM/FAIR experiment [4].

From a theoretical perspective, a high precision study of the location of the CEP is hampered by two very different problems. In lattice QCD, the fermion sign problem prohibits direct calculations at real chemical potential, see e.g. [5] for a review. Extrapolation procedures from zero chemical potential include re-weighting [6–9] and Taylor expansion schemes [10–17] allowing for indirect access to important quantities such as pseudo-critical transition temperatures, equations of state and fluctuations of conserved charges at moderate chemical potential [18]. In addition, direct lattice simulations at imaginary chemical potential provide a basis for a number of extrapolation procedures into the real chemical potential domain based on the analytic properties of the QCD partition function. This procedure has been pioneered by de Forcrand and Philipsen [19] and has been developed since, see e.g. [1, 20–23] and Refs. therein.

On the other hand, functional approaches to the CEP, i.e., approaches via Dyson–Schwinger equations (DSE) and/or the functional renormalization group (FRG), do not suffer from the sign problem and allow for a mapping of the whole QCD phase diagram, see e.g. [24] for a review and [25–30] for recent results. However, they inherently depend on approximations and truncations which have to

be carefully controlled either in combined approaches or by comparison with lattice results in controlled environments where both approaches are applicable, such as imaginary chemical potential. This work is devoted to the latter. We revisit a truncation scheme of Dyson–Schwinger equations that has been used in Ref. [30] to perform calculations at real chemical potential up to the critical endpoint and apply it at imaginary baryon chemical potential μ_B . We perform calculations at appropriate values of imaginary μ_B , where direct comparison with corresponding lattice results from Ref. [1] is possible. We then employ a similar extrapolation procedure as on the lattice and compare the extrapolated results for the crossover transition line with the ones explicitly calculated in our functional approach. Our results may serve as a quality check for the extrapolation method used on the lattice.

The paper is organized as follows. In the next section, we briefly revisit our framework. We summarize the truncation scheme of Ref. [30] in Section II A and review the extrapolation procedure from imaginary to real chemical potential employed in Ref. [1] in Section II B. In Section III, we present and discuss our results. We summarize and conclude in Section IV.

II. FRAMEWORK

A. Truncated set of coupled Dyson–Schwinger equations

The central quantity for all following investigations is the dressed quark propagator S_f of quark flavor f at non-zero temperature T and quark chemical potential μ_f .

* julian.bernhardt@physik.uni-giessen.de

† christian.fischer@theo.physik.uni-giessen.de

Its inverse is parametrized as¹

$$S_f^{-1}(p) = i\gamma_4 \tilde{\omega}_n^f C_f(p) + i\boldsymbol{\gamma} \cdot \mathbf{p} A_f(p) + B_f(p) \quad (1)$$

where $p = (\mathbf{p}, \tilde{\omega}_n)$ labels the four-momentum, while $\tilde{\omega}_n^f = \omega_n + i\mu_f$ represents a combination of the fermionic Matsubara frequencies $\omega_n = (2n + 1)\pi T$, $n \in \mathbb{Z}$, with the chemical potential. At this point, we already remark that the definition of $\tilde{\omega}_n^f$ universally holds for both real and imaginary chemical potentials in our framework. Consequently, imaginary chemical potentials effectively correspond to a real shift of the Matsubara frequencies [31, 32]. The quark dressing functions A_f , B_f and C_f in Eq. (1) encode the non-perturbative momentum dependence of the propagator.

We obtain the quark propagator as a solution of its corresponding Dyson–Schwinger equation (DSE) illustrated in Fig. 1 and given by

$$S_f^{-1}(p) = Z_2(i\gamma_4 \tilde{\omega}_n^f + i\boldsymbol{\gamma} \cdot \mathbf{p} + Z_m m_f) - \Sigma_f(p), \quad (2)$$

with Z_2 and Z_m labelling the wave function and mass renormalization constants, respectively, which are calculated in vacuum using a momentum-subtraction scheme. Additionally, m_f denotes the flavor-dependent current quark mass. The quark self-energy reads

$$\Sigma_f(p) = (ig)^2 \frac{4}{3} \frac{Z_2}{\tilde{Z}_3} T \sum_{\omega_n} \int \frac{d^3 q}{(2\pi)^3} D_{\nu\rho}(p-q) \gamma_\nu \times S_f(q) \Gamma_\rho^f(p, q; p-q)_Q, \quad (3)$$

where g denotes the strong coupling constant, \tilde{Z}_3 the ghost renormalization constant and $D_{\nu\rho}$ the dressed gluon propagator. The two factors of ig are pulled out of the vertices such that Γ_ρ^f represents the reduced dressed quark–gluon vertex. The trace over color space, which was already performed, results in the prefactor of $4/3$ for $N_c = 3$ colors.

Solving the quark DSE requires knowledge about the gluon $D_{\nu\rho}$ and the quark–gluon vertex Γ_ρ^f . As in Ref. [30], we use the truncation for the gluon DSE shown in Fig. 1, where all Yang–Mills diagrams (one- and two-loop diagrams with ghosts and gluons only) are replaced by an inverse quenched gluon propagator that is reconstructed from temperature-dependent fits to results of quenched lattice calculations [33–35]. Denoting the quenched gluon by $D_{\nu\rho}^{\text{YM}}$, the truncated gluon DSE is given by

$$D_{\nu\rho}^{-1}(p) = [D_{\nu\rho}^{\text{YM}}(p)]^{-1} + \Pi_{\nu\rho}(p). \quad (4)$$

Here, $\Pi_{\nu\rho}$ represents the quark loop that is evaluated explicitly and reads

$$\Pi_{\nu\rho}(p) = \frac{(ig)^2}{2} \sum_f \frac{Z_2}{\tilde{Z}_3} T \sum_{\omega_n} \int \frac{d^3 q}{(2\pi)^3} \text{Tr}[\gamma_\nu S_f(q) \times \Gamma_\rho^f(q-p, q; p)_G S_f(q-p)], \quad (5)$$

where the prefactor of $1/2$ again originates in the color trace. The flavor sum f runs over $N_f = 2+1$ quark flavors, i.e., we work with up, down and strange quarks. The influence of the charm quark on the QCD phase diagram has been addressed in [25] and found to be negligible. The explicit inclusion of the quark loop generates an unquenched gluon with contributions from all active quark flavors. Consequently, the different quarks also influence each other indirectly via the gluon.

The last quantity we need in order to render the previous set of equations self-contained is the quark–gluon vertex Γ_ρ^f . As in Ref. [30], we employ a slightly different form of the vertex in the quark self-energy and in the quark loop, indicated by subscripts Q and G in Eqs. (3) and (5), respectively. Our ansatz reads:

$$\Gamma_\rho^f(p, q; k)_Q = Z_2^f \gamma_\rho \Gamma(k^2), \quad (6)$$

$$\Gamma_\rho^f(p, q; k)_G = \Gamma_\rho^{f, \text{BC}}(p, q) \Gamma(q^2 + p^2). \quad (7)$$

Here,

$$\Gamma_\rho^{f, \text{BC}}(p, q) = \delta_{\rho i} \gamma^i \frac{A_f(p) + A_f(q)}{2} + \delta_{\rho 4} \gamma^4 \frac{C_f(p) + C_f(q)}{2} \quad (8)$$

denotes the leading Dirac tensor structure of the Ball–Chiu vertex [36] which incorporates to backcoupling effects of the quarks onto the vertex, while

$$\Gamma(x) = \frac{d_1}{d_2 + x} + \frac{x}{\Lambda^2 + x} \left(\frac{\alpha(\nu)\beta_0}{4\pi} \ln(x/\Lambda^2 + 1) \right)^{2\delta} \quad (9)$$

labels a phenomenological vertex dressing function. It consists of an enhancement at small momenta (IR) inspired by Slavnov–Taylor identities while it ensures the correct perturbative behavior of the propagators in the UV at large momenta. The running coupling at the renormalization point $\nu = 80$ GeV reads $\alpha(\nu) = 0.3$, the scales $d_2 = 0.5$ GeV² and $\Lambda = 1.4$ GeV are fixed to match the ones in the gluon lattice data, and the anomalous dimension is given by $\delta = -9N_c/(44N_c - 8N_f)$, while $\beta_0 = (11N_c - 2N_f)/3$. We work in a setup of $N_f = 2 + 1$ quark flavors, i.e., the isospin-symmetric limit of degenerate up and down quarks ($m_u = m_d$, $\mu_u = \mu_d$). Furthermore, we choose $\mu_s = 0$ such that the baryon chemical potential is given by $\mu_B = 3\mu_u$. The quark masses have been determined in Ref. [37] in the vacuum using the experimental pion and kaon masses. This leads to values of $m_u = 1.47$ MeV and $m_s = 37.8$ MeV at a renormalization point of 80 GeV. The vertex strength parameter d_1 for this truncation has been determined in Refs. [30, 37] to obtain a pseudocritical temperature at vanishing chemical potential consistent with lattice results for the subtracted condensate. In this work, we use a slightly different value that is adapted to the conventions used in [1] for the determination of the pseudocritical temperature (see below for details). This leads to $d_1 = 12.71$ GeV² (instead of

¹ We work in Euclidean space-time with positive metric signature (++++). The Hermitian γ -matrices satisfy $\{\gamma_\nu, \gamma_\rho\} = 2\delta_{\nu\rho}$.

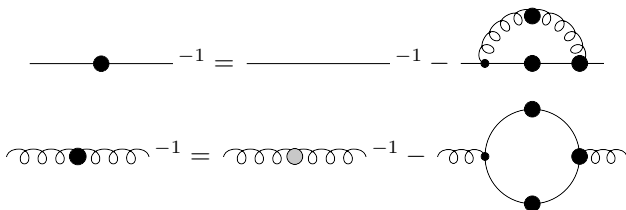


FIG. 1. DSE for the quark propagator (top) and truncated gluon DSE (bottom). Large filled dots indicate dressed quantities; solid and curly lines represent quark and gluon propagators, respectively. There is a separate DSE for each flavor. The large gray dot denotes the quenched gluon propagator that is taken from the lattice while the quark loop is evaluated explicitly. The latter contains an implicit flavor sum.

$d_1 = 12.85 \text{ GeV}^2$ as in [30]) in the quark self-energy and 8.49 GeV^2 (same as in [30]) in the quark loop.

With this input, we solve the set of quark and gluon DSEs self-consistently in the same numerical setup as described in more detail in Refs. [26, 38] and thus obtain the quark and gluon propagators as well as quark number and higher susceptibilities for arbitrary temperatures and (real or imaginary) chemical potentials.

B. Extrapolating from imaginary to real chemical potential

In the following, we detail the extrapolation procedure of Ref. [1] based on results for the up quark condensate $\langle \bar{\psi}\psi \rangle$ and the chiral susceptibility χ at imaginary chemical potential and adapt it to our DSE framework.

With the solutions for the coupled set of DSEs (displayed in Fig. 1) at hand, we are able to determine the up-quark condensate straightforwardly from its propagator via taking appropriate traces. The corresponding quark susceptibility is defined as its derivative with respect to the quark mass:

$$\langle \bar{\psi}\psi \rangle(T) = 3Z_2^f Z_m T \sum_{\omega_k} \int_{\mathbf{q}} \text{Tr}[S_u(q)], \quad (10)$$

$$\chi(T) = \frac{\partial \langle \bar{\psi}\psi \rangle(T)}{\partial m_u}. \quad (11)$$

The quark susceptibility is numerically determined in our approach via a finite-difference formula.²

The expression for the condensate in Eq. 10 is divergent and needs to be regularized. Similar to Ref. [1], we define the regularized condensate and susceptibility in the

² In principle, one could also determine the derivative directly, but this is about an order of magnitude more involved in terms of CPU-time. We have tested the quality of the finite difference method in comparable cases and found it to be accurate on the sub-percent level.

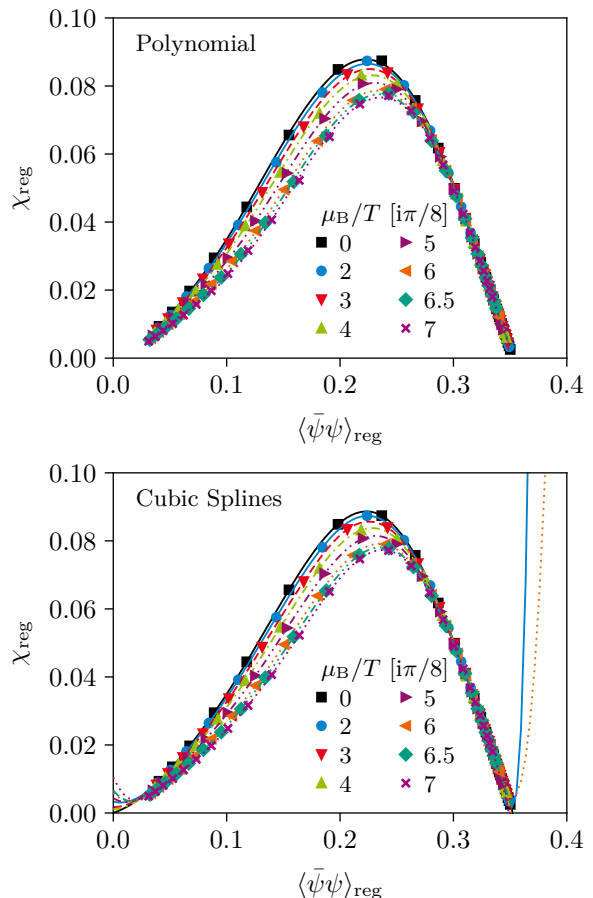


FIG. 2. Chiral susceptibility as a function of the chiral condensate for imaginary chemical potentials. The points indicate the DSE data while the curves represent polynomial fits (upper panel) or cubic spline interpolations (lower panel), respectively.

following way:

$$\langle \bar{\psi}\psi \rangle_{\text{reg}}(T) = [\langle \bar{\psi}\psi \rangle(T) - \langle \bar{\psi}\psi \rangle(0)] \frac{m_u}{f_\pi^4}, \quad (12)$$

$$\chi_{\text{reg}}(T) = [\chi(T) - \chi(0)] \frac{m_u^2}{f_\pi^4}, \quad (13)$$

where $f_\pi = 130.41 \text{ MeV}$ indicates the pion decay constant in the vacuum.

Utilizing these definitions, we determine the pseudo-critical transition temperature as follows:

1. We calculate the regularized condensate $\langle \bar{\psi}\psi \rangle(T)$ and susceptibility $\chi(T)$ for a discrete set of temperatures at each value of imaginary/real chemical potential.
2. This data is converted to a discrete set of points with the dependence $\chi(\langle \bar{\psi}\psi \rangle)$.
3. We use either a fit to a polynomial of order five or a cubic spline interpolation to determine the peak position of these curves. This yields the value of

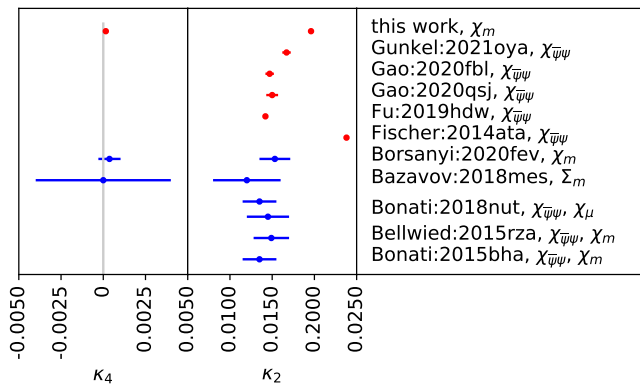


FIG. 3. Expansion coefficients κ_2 and κ_4 for the pseudocritical chiral transition line parametrized in Eq.(14) from different sources. Lattice QCD results [1, 39–42] are in blue, DSE/FRG results [25, 27–30] in red.

the condensate at the pseudocritical temperature $\langle\bar{\psi}\psi\rangle(T_c)$.

4. Going back to the discrete set of values for $\langle\bar{\psi}\psi\rangle(T)$ determined in step one, we use an appropriate interpolation procedure to extract T_c from $\langle\bar{\psi}\psi\rangle(T_c)$.

III. RESULTS AND DISCUSSION

In Fig. 2, we display the datasets and resulting curves of $\chi(\langle\bar{\psi}\psi\rangle)$ obtained from steps 2 and 3 (defined at the end of the last section) for imaginary chemical potentials in the range $\mu_B/T = (0, \dots, 7) \times i\pi/8$. The points indicate DSE data, while the curves represent polynomial fits in the upper panel and cubic spline interpolations in the lower panel, respectively.

We first notice that both the polynomial fits and the cubic splines match the DSE data almost perfectly and yield very similar results. In fact, this observation holds true for real chemical potentials up to rather large values. As a consequence and for the sake of comparability with the lattice results, we restrict ourselves to the polynomial fit results except when noted otherwise.

From Fig. 2 it is obvious that our curves $\chi(\langle\bar{\psi}\psi\rangle)$ at different rescaled imaginary chemical potential μ_B/T are close to each other, but do not collapse to one curve. We rather find that both peak height and peak position vary slightly with imaginary μ_B . That is, the peak position is at the largest χ but smallest $\langle\bar{\psi}\psi\rangle$ for $\mu_B/T = 0$ while it moves to smallest χ but largest $\langle\bar{\psi}\psi\rangle$ for $\mu_B/T = 7/8\pi i$. We therefore do not confirm the apparent collapse (within error bars) observed in Ref. [1], however without attaching great significance to this observation. Indeed, in later works, μ_B -dependent corrections to simple rescaling laws have been successfully explored [20, 23].

In the next step, we gauge the quality of extrapolations from imaginary to real chemical potentials. In the DSE approach, this is possible since explicit results at

real chemical potential have been determined already in Ref. [30] and have been verified by us independently for this work. Using first the inflection point of the subtracted condensate as crossover criterion, the phase diagram for the setup of Ref. [30] (“previous work”) and the one of this work with the slightly adapted vertex strength parameter d_1 (“inflection point”) are shown in Fig. 4. We find an almost uniformly shifted phase boundary to slightly lower temperatures as expected due to the reduced vertex strength. Using the peak of the susceptibility, Eq. (12), as criterion, we find a crossover line at somewhat larger temperatures that merges with the previous one, of course, at the critical endpoint. The fits to the condensate using polynomials as well as the cubic spline interpolations end up in very similar results.

Now we are in a position to compare results obtained from extrapolations with explicitly calculated results. To this end, we fit our results for the phase boundary at imaginary chemical potentials to the well-known parametrization of the pseudocritical transition temperature:

$$\frac{T_c(\mu_B)}{T_c} = 1 - \kappa_2 \left(\frac{\mu_B}{T_c} \right)^2 - \kappa_4 \left(\frac{\mu_B}{T_c} \right)^4, \quad (14)$$

where $T_c = T_c(\mu_B = 0)$ and κ_2 labels the curvature. In the left half of the lower diagram of Fig. 4, we illustrate the pseudocritical temperature obtained for polynomial fits at imaginary chemical potentials. The blue square boxes show the results of the DSE calculations, while the black curve indicates the fit to the parametrization given in Eq. (14). The resulting fit parameters are given by:

$$\kappa_2^{\text{poly}} = 0.0196 \pm 0.0001, \quad \kappa_4^{\text{poly}} = 0.00015 \pm 0.00001, \quad (15)$$

with very small error and almost vanishing χ^2 -value due to the non-statistical nature of the data. The fit very accurately represents the DSE data. If we use cubic spline interpolations, we again end up at very similar results, i.e., $\kappa_2^{\text{spln}} = 0.0196 \pm 0.0001$ and $\kappa_4^{\text{spln}} = 0.00014 \pm 0.00001$. This underpins the fact that at imaginary chemical potentials, our data points are very well represented by the polynomial fit. The difference of the values for κ_2 in Eq. (15) as compared to

$$\kappa_2^{\text{infl}} = 0.0173 \quad (16)$$

presented in Ref. [30] and obtained in the same truncation scheme as used in this work is entirely due to the difference in the definition of the pseudocritical temperature from a different regularized order parameter. The resulting shifts of the transition lines seen in the upper diagram of Fig. 4 has been discussed above. Since pseudo-critical transition lines from different definitions all end up in the same critical endpoint they naturally have different curvature. For completeness, we show results from different sources in Fig. 3 and the resulting critical end point for the DSE/FRG calculations in the upper right diagram of Fig. 4.

Now, we can analytically continue this fit to real chemical potential and compare to DSE results obtained there.

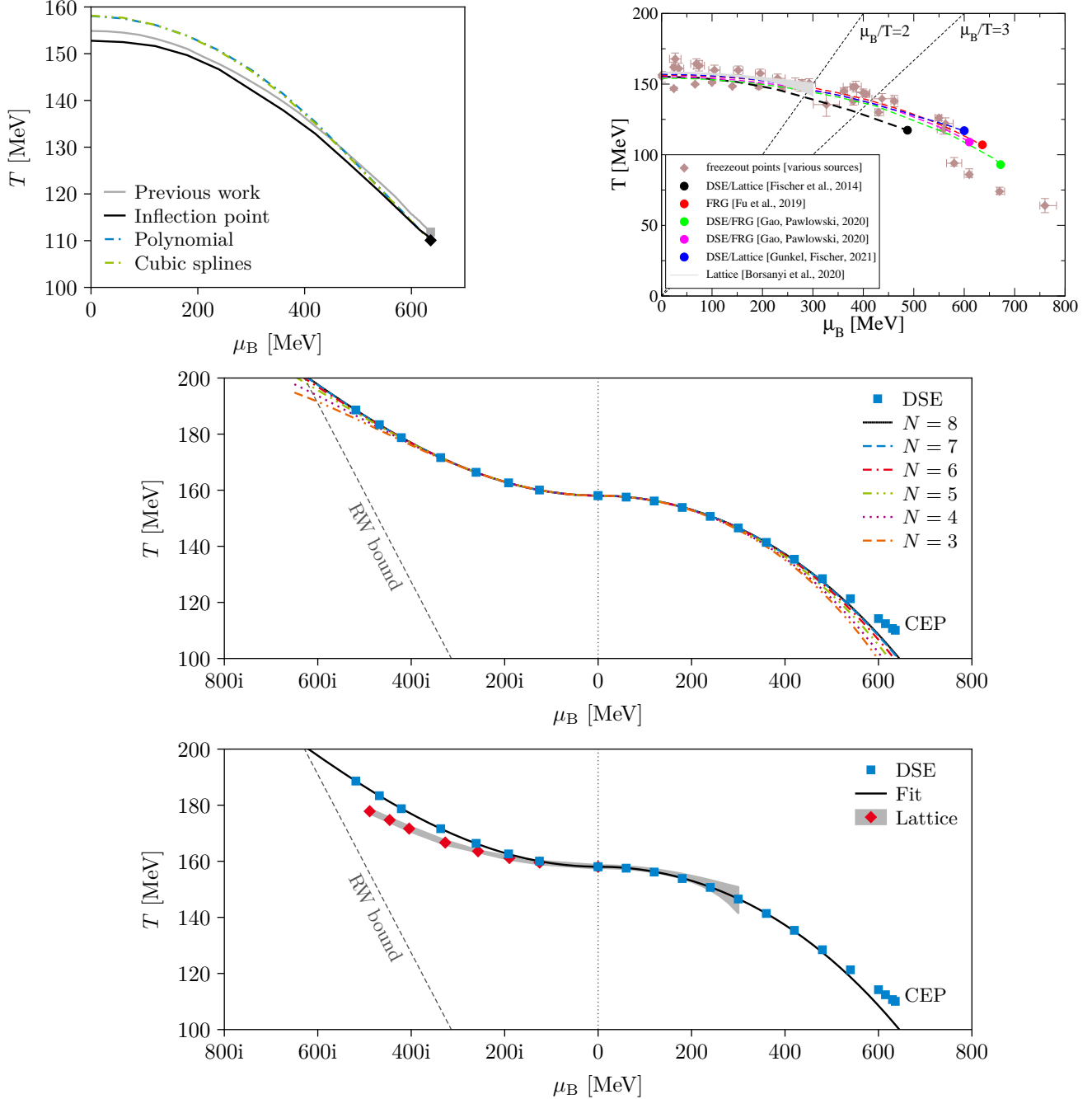


FIG. 4. Upper left diagram: Phase diagram for different definitions of the pseudocritical temperature (see main text for explanations). Upper right diagram: Phase diagram with critical end point determined in different truncation schemes for DSEs and FRGs [25, 27–30]. Middle diagram: Results for fits to different numbers of point at imaginary potential. N counts the number of points starting with 1 at zero chemical potential and adding point by point in the direction of large imaginary chemical potential. Lower diagram: Pseudocritical transition temperature at both imaginary and real chemical potentials from DSEs (points) and fit (line). The gray band and the red diamonds correspond to the lattice results from Ref. [1].

This is done and displayed in the middle diagram of Fig. 4. Starting with fits to data at zero chemical potential and the two lowest imaginary chemical potential values $N = 3$, we add point by point in the direction of large imaginary

chemical potential until we included all data at $N = 8$. We clearly observe that in the quality of the fits improve rapidly until it settles down at about $N = 6$. Adding further points brings only very small improvement. We

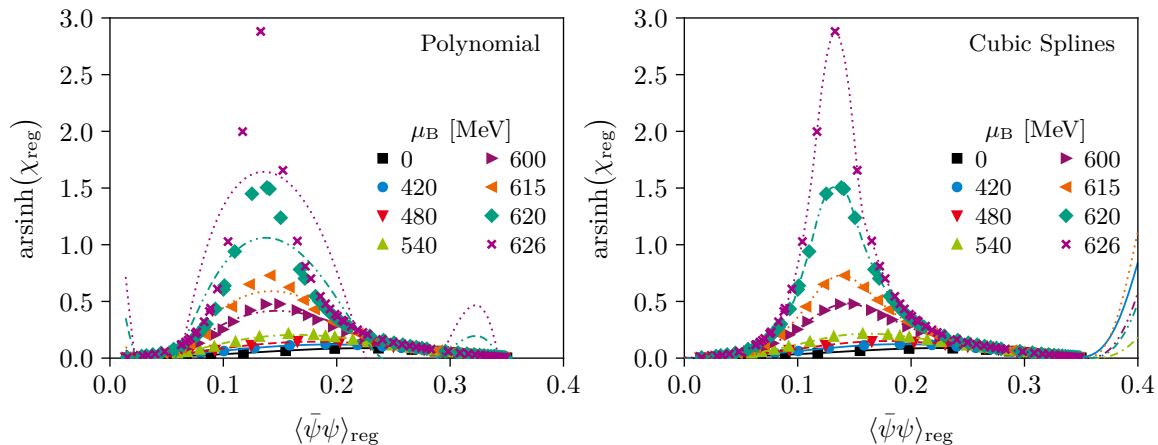


FIG. 5. Chiral susceptibility as a function of the chiral condensate for real chemical potentials near the CEP. The points indicate the DSE data while the curves represent polynomial fits (left panel) or cubic spline interpolations (right panel), respectively.

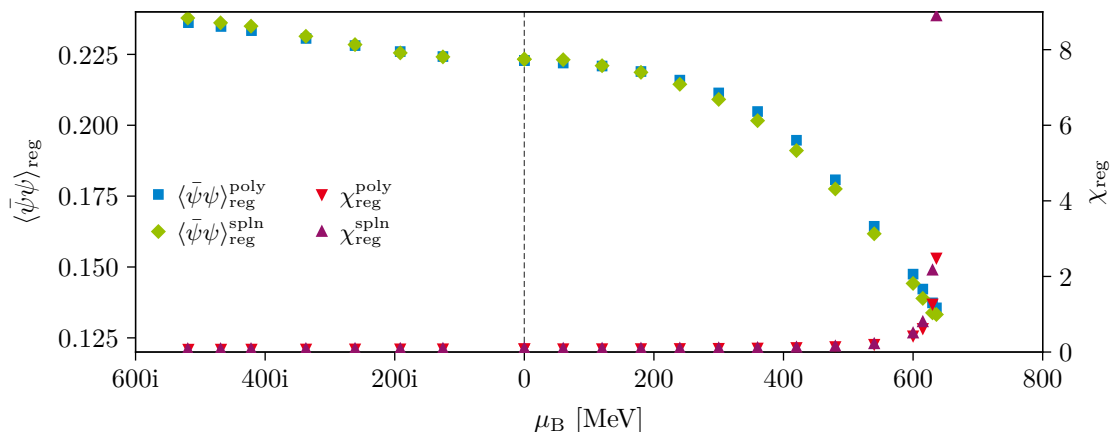


FIG. 6. Condensate (blue and green) and susceptibility (red and purple) at the pseudocritical temperature for both imaginary and real chemical potentials obtained with both polynomial fits and cubic spline interpolations.

conclude from this that going deep in the imaginary chemical potential region is important, but one does not need to go all the way to the Roberge-Weiss bound. We could have stopped at $N = 6$. We furthermore checked that leaving out two arbitrary points in between the one with largest imaginary chemical potential and the one with zero chemical potential does not change the quality of the fit at all.

In the lower diagram of Fig. 4, we show our best fit result together with the lattice data of Ref. [1] (red diamonds) and their fit result (grey band). The discrepancy of our data and the lattice data at large imaginary chemical potential is a measure of the systematic error of our calculation and therefore of our data points. This systematic error is small by construction in the vicinity of zero chemical potential, but grows into the five percent region for largest imaginary chemical potential. (Naively) assuming the error to be symmetric in μ_B , our CEP could be accurate on the level of ten percent. But, of course, we cannot exclude that new physics effects at large real chemical potential might invalidate this naive estimate.

In general, we observe a remarkable coincidence between our fit and the DSE data up to rather large chemical potentials. Deviations of more than one percent in temperature occur only for $\mu_B > 510$ MeV, i.e. for chemical potential larger than 80 % of the one of the CEP, which in the present truncation is located at around $\mu_B^{\text{CEP}} \approx 636$ MeV. We can infer that the extrapolation from imaginary chemical potentials works excellently for a large part of the crossover region well towards the CEP.

In vicinity of the CEP, however, not only does the extrapolation of T_c cease to be valid, the $\chi(\langle\bar{\psi}\psi\rangle)$ curves also can no longer be approximated by a polynomial as is illustrated in Fig. 5. There, we show the chiral susceptibility as a function of the chiral condensate analogously to Fig. 2, this time for real chemical potentials $\mu_B > 420$ MeV and $\mu_B = 0$ as a reference. We depict the polynomial fits and cubic spline interpolations in the left and right panels, respectively. Obviously, the approximation of a fifth-order polynomial breaks down completely at around $\mu_B \gtrsim 600$ MeV. In this region, only the splines reliably coincide with the DSE data.

This discrepancy is also visible in Fig. 6, where we plot peak height and peak position of $\chi(\langle\psi\psi\rangle)$ as a function of negative and positive values of $(\mu_B/T)^2$ in Fig. 6. We show results for the polynomial fits as well as the cubic spline interpolations for the sake of comparison. We notice again that both peak position and height are not entirely constant at imaginary chemical potentials in slight contrast to the lattice results discussed in Ref. [1]. While the change of the condensate is more or less constant for real μ_B , the critical susceptibility does not change much for small chemical potentials but drastically in vicinity of the CEP as expected. This is also the region where the polynomial fit and the spline interpolation deviate substantially, i.e., where the assumption of a low order polynomial breaks down. Again, this is to be expected since the susceptibility is singular at the CEP.

We would like to finish our analysis by pointing out that our results fully support the analysis performed in Ref. [1]. In the imaginary chemical potential region where the lattice fits have been done, there is no difference in quality in using polynomial or spline fits. This is also true for the region of real chemical potential covered by the lattice extrapolation. The (expected) problems with the polynomial fits emerge only at much larger real chemical potential, close to the CEP.

IV. SUMMARY AND CONCLUSIONS

In this work, we have studied whether the extrapolation procedure from imaginary to real chemical potential introduced in Ref. [1] in the context of lattice QCD is capable to reproduce explicit results for the phase transition line at real chemical potential obtained with functional methods. The result is very encouraging: up to quite

large chemical potentials not very much smaller ($\approx 20\%$) than the one of the critical endpoint, the extrapolation works extremely well. For larger chemical potential, the extrapolated transition line undershoots the calculated one; at the critical chemical potential $\mu_B^{\text{CEP}} \approx 636$ MeV, the resulting temperature of the extrapolation is about 13 MeV too small. Also, of course, it is not possible to extract the location of the CEP from the extrapolation procedure. However, comparing the lattice results with the ones of our framework at large imaginary chemical potential and taking this as a (naive) measure for the corresponding systematic error of our framework at corresponding values for real chemical potential, this indicates a systematic error of the order of 5-10 percent for the location of the CEP.

An interesting option is to study the different extrapolation procedure brought forward in [21]. An interesting further option is to directly determine the location of Lee-Young zeros. This is relegated to future work.

ACKNOWLEDGMENTS

We thank both, Jana N. Guenther and Philipp Isserstedt for enlightening discussions. We furthermore thank Jana N. Guenther for providing the lattice data for comparison and Philipp Isserstedt for crosschecks of the numerical code at an early stage of this work. This work has been supported by the Helmholtz Graduate School for Hadron and Ion Research (HGS-HIRE) for FAIR, the GSI Helmholtzzentrum für Schwerionenforschung and the Deutsche Forschungsgemeinschaft (DFG, German Research Foundation) through the Collaborative Research Center TransRegio CRC-TR 211 “Strong-interaction matter under extreme conditions”. Feynman diagrams were drawn with JAXODRAW [43].

-
- [1] S. Borsányi *et al.*, QCD Crossover at Finite Chemical Potential from Lattice Simulations, *Phys. Rev. Lett.* **125**, 052001 (2020), arXiv:2002.02821 [hep-lat].
 - [2] A. Bzdak *et al.*, Mapping the phases of quantum chromodynamics with beam energy scan, *Phys. Rep.* **853**, 1 (2020), arXiv:1906.00936 [nucl-th].
 - [3] P. Salabura and J. Stroth, Dilepton radiation from strongly interacting systems, *Prog. Part. Nucl. Phys.* **120**, 103869 (2021), arXiv:2005.14589 [nucl-ex].
 - [4] B. Friman *et al.*, eds., *The CBM Physics Book: Compressed Baryonic Matter in Laboratory Experiments*, Lecture Notes in Physics No. 814 (Springer, 2011).
 - [5] K. Nagata, Finite-density lattice QCD and sign problem: Current status and open problems, *Prog. Part. Nucl. Phys.* **127**, 103991 (2022), arXiv:2108.12423 [hep-lat].
 - [6] A. Hasenfratz and D. Toussaint, Canonical ensembles and nonzero density quantum chromodynamics, *Nucl. Phys. B* **371**, 539 (1992).
 - [7] Z. Fodor and S. D. Katz, A New method to study lattice QCD at finite temperature and chemical potential, *Phys. Lett. B* **534**, 87 (2002), arXiv:hep-lat/0104001.
 - [8] Z. Fodor and S. D. Katz, Lattice determination of the critical point of QCD at finite T and mu, *JHEP* **03**, 014, arXiv:hep-lat/0106002.
 - [9] M. Giordano, K. Kapas, S. D. Katz, D. Negradi, and A. Pasztor, New approach to lattice QCD at finite density; results for the critical end point on coarse lattices, *JHEP* **05**, 088, arXiv:2004.10800 [hep-lat].
 - [10] C. R. Allton, S. Ejiri, S. J. Hands, O. Kaczmarek, F. Karsch, E. Laermann, C. Schmidt, and L. Scorzato, The QCD thermal phase transition in the presence of a small chemical potential, *Phys. Rev. D* **66**, 074507 (2002), arXiv:hep-lat/0204010.
 - [11] R. V. Gavai and S. Gupta, QCD at finite chemical potential with six time slices, *Phys. Rev. D* **78**, 114503 (2008), arXiv:0806.2233 [hep-lat].
 - [12] S. Borsanyi, G. Endrodi, Z. Fodor, S. D. Katz, S. Krieg, C. Ratti, and K. K. Szabo, QCD equation of state at nonzero chemical potential: continuum results with physical quark masses at order mu^2 , *JHEP* **08**, 053, arXiv:1204.6710 [hep-lat].
 - [13] A. Bazavov *et al.*, The QCD Equation of State to $\mathcal{O}(\mu_B^6)$

- from Lattice QCD, *Phys. Rev. D* **95**, 054504 (2017), arXiv:1701.04325 [hep-lat].
- [14] M. Giordano, K. Kapas, S. D. Katz, D. Negradi, and A. Pasztor, Radius of convergence in lattice QCD at finite μ_B with rooted staggered fermions, *Phys. Rev. D* **101**, 074511 (2020), [Erratum: *Phys.Rev.D* 104, 119901 (2021)], arXiv:1911.00043 [hep-lat].
- [15] A. Bazavov *et al.* (HotQCD), Chiral crossover in QCD at zero and non-zero chemical potentials, *Phys. Lett. B* **795**, 15 (2019), arXiv:1812.08235 [hep-lat].
- [16] A. Bazavov *et al.*, Skewness, kurtosis, and the fifth and sixth order cumulants of net baryon-number distributions from lattice QCD confront high-statistics STAR data, *Phys. Rev. D* **101**, 074502 (2020), arXiv:2001.08530 [hep-lat].
- [17] D. Bollweg, J. Goswami, O. Kaczmarek, F. Karsch, S. Mukherjee, P. Petreczky, C. Schmidt, and P. Scior (HotQCD), Taylor expansions and Padé approximants for cumulants of conserved charge fluctuations at nonvanishing chemical potentials, *Phys. Rev. D* **105**, 074511 (2022), arXiv:2202.09184 [hep-lat].
- [18] C. Ratti, Equation of state for QCD from lattice simulations, *Prog. Part. Nucl. Phys.* **129**, 104007 (2023).
- [19] P. de Forcrand and O. Philipsen, The QCD phase diagram for small densities from imaginary chemical potential, *Nucl. Phys. B* **642**, 290 (2002), arXiv:hep-lat/0205016.
- [20] S. Borsányi *et al.*, Lattice QCD Equation of State at Finite Chemical Potential from an Alternative Expansion Scheme, *Phys. Rev. Lett.* **126**, 232001 (2021), arXiv:2102.06660 [hep-lat].
- [21] P. Dimopoulos, L. Dini, F. Di Renzo, J. Goswami, G. Nicotra, C. Schmidt, S. Singh, K. Zambello, and F. Ziesché, Contribution to understanding the phase structure of strong interaction matter: Lee-Yang edge singularities from lattice QCD, *Phys. Rev. D* **105**, 034513 (2022), arXiv:2110.15933 [hep-lat].
- [22] S. Borsanyi, Z. Fodor, M. Giordano, J. N. Guenther, S. D. Katz, A. Pasztor, and C. H. Wong, Equation of state of a hot-and-dense quark gluon plasma: lattice simulations at real μ_B vs. extrapolations, (2022), arXiv:2208.05398 [hep-lat].
- [23] S. Borsanyi, J. N. Guenther, R. Kara, Z. Fodor, P. Parotto, A. Pasztor, C. Ratti, and K. K. Szabo, Resummed lattice QCD equation of state at finite baryon density: Strangeness neutrality and beyond, *Phys. Rev. D* **105**, 114504 (2022), arXiv:2202.05574 [hep-lat].
- [24] C. S. Fischer, QCD at finite temperature and chemical potential from Dyson–Schwinger equations, *Prog. Part. Nucl. Phys.* **105**, 1 (2019), arXiv:1810.12938 [hep-ph].
- [25] C. S. Fischer, J. Luecker, and C. A. Welzbacher, Phase structure of three and four flavor QCD, *Phys. Rev. D* **90**, 034022 (2014), arXiv:1405.4762 [hep-ph].
- [26] P. Isserstedt, M. Buballa, C. S. Fischer, and P. J. Gunkel, Baryon number fluctuations in the QCD phase diagram from Dyson–Schwinger equations, *Phys. Rev. D* **100**, 074011 (2019), arXiv:1906.11644 [hep-ph].
- [27] W.-j. Fu, J. M. Pawłowski, and F. Rennecke, QCD phase structure at finite temperature and density, *Phys. Rev. D* **101**, 054032 (2020), arXiv:1909.02991 [hep-ph].
- [28] F. Gao and J. M. Pawłowski, QCD phase structure from functional methods, *Phys. Rev. D* **102**, 034027 (2020), arXiv:2002.07500 [hep-ph].
- [29] F. Gao and J. M. Pawłowski, Chiral phase structure and critical end point in QCD, *Phys. Lett. B* **820**, 136584 (2021), arXiv:2010.13705 [hep-ph].
- [30] P. J. Gunkel and C. S. Fischer, Locating the critical endpoint of QCD: Mesonic backcoupling effects, *Phys. Rev. D* **104**, 054022 (2021), arXiv:2106.08356 [hep-ph].
- [31] J. Braun, L. M. Haas, F. Marhauser, and J. M. Pawłowski, Phase Structure of Two-Flavor QCD at Finite Chemical Potential, *Phys. Rev. Lett.* **106**, 022002 (2011), arXiv:0908.0008 [hep-ph].
- [32] C. S. Fischer, J. Luecker, and J. M. Pawłowski, Phase structure of QCD for heavy quarks, *Phys. Rev. D* **91**, 014024 (2015), arXiv:1409.8462 [hep-ph].
- [33] C. S. Fischer, A. Maas, and J. A. Mueller, Chiral and deconfinement transition from correlation functions: SU(2) vs. SU(3), *Eur. Phys. J. C* **68**, 165 (2010), arXiv:1003.1960 [hep-ph].
- [34] A. Maas, J. M. Pawłowski, L. von Smekal, and D. Spielmann, The gluon propagator close to criticality, *Phys. Rev. D* **85**, 034037 (2012), arXiv:1110.6340 [hep-lat].
- [35] G. Eichmann, C. S. Fischer, and C. A. Welzbacher, Baryon effects on the location of QCD’s critical end point, *Phys. Rev. D* **93**, 034013 (2016), arXiv:1509.02082 [hep-ph].
- [36] J. S. Ball and T.-W. Chiu, Analytic properties of the vertex function in gauge theories. I, *Phys. Rev. D* **22**, 2542 (1980).
- [37] P. J. Gunkel, C. S. Fischer, and P. Isserstedt, Quarks and light (pseudo-)scalar mesons at finite chemical potential, *Eur. Phys. J. A* **55**, 169 (2019), arXiv:1907.08110 [hep-ph].
- [38] P. Isserstedt, *Thermodynamics of strong-interaction matter: On the phase structure and thermodynamics of quantum chromodynamics with Dyson–Schwinger equations*, Ph.D. thesis, Giessen University, Germany (2021).
- [39] C. Bonati, M. D’Elia, M. Mariti, M. Mesiti, F. Negro, and F. Sanfilippo, Curvature of the chiral pseudocritical line in qcd: Continuum extrapolated results, *Phys. Rev. D* **92**, 054503 (2015), arXiv:1507.03571 [hep-lat].
- [40] R. Bellwied *et al.*, The QCD phase diagram from analytic continuation, *Phys. Lett. B* **751**, 559 (2015), arXiv:1507.07510 [hep-lat].
- [41] C. Bonati, M. D’Elia, F. Negro, F. Sanfilippo, and K. Zambello, Curvature of the pseudocritical line in qcd: Taylor expansion matches analytic continuation, *Phys. Rev. D* **98**, 054510 (2018), arXiv:1805.02960 [hep-lat].
- [42] A. Bazavov *et al.* (HotQCD), Chiral crossover in qcd at zero and non-zero chemical potentials, *Phys. Lett. B* **795**, 15 (2019), arXiv:1812.08235 [hep-lat].
- [43] D. Binosi, J. Collins, C. Kaufhold, and L. Theussl, Jaxo-Draw: A graphical user interface for drawing Feynman diagrams. Version 2.0 release notes, *Comput. Phys. Commun.* **180**, 1709 (2009), arXiv:0811.4113 [hep-ph].